Signal Processing 137 (2017) 124–134

Contents lists available at ScienceDirect

Signal Processing

journal homepage: www.elsevier.com/locate/sigpro

Off-grid DOA estimation in real spherical harmonics domain using sparse Bayesian inference

Qinghua Huang*, Longfei Xiang, Kai Liu

Key Laboratory of Specialty Fiber Optics and Optical Access Networks, Shanghai University, Shanghai 200072, China

ARTICLE INFO

Article history:
Received 15 April 2016
Revised 14 December 2016
Accepted 30 January 2017
Available online 7 February 2017

Keywords:
Direction-of-arrival (DOA) estimation
Sparse Bayesian inference
2-D off-grid model
Real spherical harmonics
Least squares

ABSTRACT

When true targets do not locate exactly on discretized sampling grids, sparse reconstruction methods cannot estimate direction-of-arrival (DOA) accurately due to angular differences. This DOA estimation problem can be solved by off-grid sparse Bayesian inference (OGSBI). However, this method brings high computational complexity when estimating 2-D off-grid DOAs with spherical arrays. In order to solve 2-D off-grid DOA estimation, we adopt two steps to reduce computations and meanwhile maintain good performance. First, a real-valued off-grid model is constructed in real spherical harmonics domain. It models angular differences by exploiting the multivariable Taylor expansion to construct a matching matrix. Second, a projection-based basis selection sparse Bayesian learning combining with least squares (PSBL-LS) algorithm is proposed to estimate 2-D off-grid DOAs. This method reduces computations in learning both posterior of sparse signals and angular differences. The PSBL-LS uses the potential basis functions selected from the matching matrix to learning the posterior distribution of sparse signals. At the same time, the angular differences are estimated by least squares method based on the selected basis functions. Simulations show our proposed method improves accuracy and reduces computational load.

1. Introduction

Direction-of-arrival (DOA) estimation is an active research field of array signal processing and has been used in various applications, such as localization of transmitting sources, channel modeling, tracking, and surveillance [1, 2]. The classical subspace methods include multiple signal classification (MUSIC) [3] and estimating signal parameter via rotational invariance techniques (ESPRIT) [4]. However, these methods either require a large number of snapshots or a special structure of the array and they cannot provide high accuracy. Recently, sparse reconstruction has been used in DOA estimation because the signals impinging on the arrays are intrinsically sparse in the spatial domain [5-8]. It does not need many snapshots and can achieve higher accuracy. Different from l_1-norm minimization based reconstruction algorithms [9, 10], sparse Bayesian learning (SBL) can acquire the sparsest solution and improve the DOA estimation accuracy [11–14]. However, when DOAs are estimated using sparse reconstruction algorithms, the spatial angle must be sampled by a finite number of candidate grids and a measurement matrix is constructed based on these grids. In applications, DOAs may not locate on these fixed grids which can cause mismatch between the adopted measurement matrix and the actual one. Therefore, there are mismatching errors between the estimated angles and the true ones. This situation is called off-grid DOA estimation [18–24].

Researchers proposed some solutions to solve mismatching problems. One kind of method is continuous parameter estimation using atomic norm minimization [15–20]. This method needs to construct unique semi-definite program according to different application scenarios and use convex optimization to recover the interested signals. Another kind of methods are constructing a matching matrix based on perturbations or linear approximation [21–22]. Zhu et al. [21] introduced a sparse total least squares method to reduce the gap between the true DOA and its corresponding nearest grid. This method is only feasible when the gap is Gaussian distribution. In [22], joint sparsity was achieved by using joint orthogonal matching pursuit (J-OMP) method to estimate off-grid DOAs. In this way, the dimension of the measurement matrix has been expanded greatly because J-OMP needs to vectorize the covariance matrix of received signals. In [23, 24], the off-grid DOA estimation problem was solved by OGSBI-SVD and OGBSBL from the Bayesian perspective. The posterior distribution of sparse signals was estimated by sparse Bayesian inference and the hyper-parameters were updated by point estimates. The angular differences were estimated by expectation-maximization (EM) algorithm. But the computational complexity is high if we use SBL inference in [23] to estimate 2-D off-grid DOAs with spherical arrays directly.

* Corresponding author.
E-mail address: qinghua@shu.edu.cn (Q. Huang).

http://dx.doi.org/10.1016/j.sigpro.2017.01.035
0165-1684/

In order to decrease the complexity, two kinds of approaches were proposed. One method is transforming complex-valued models to real-valued models. Based on l_1-norm and singular value decomposition (SVD), Dai et al. proposed a real-valued l_1-SVD method for uniform linear arrays (ULAs) in order to reduce the amount of computations [25, 26]. Si et al. proposed the real-valued sparse Bayesian method for off-grid DOA estimation for ULAs [27]. These methods use the centrohermitian property of the measurement matrix and are only suitable for ULAs. Huang et al. proposed a method to transform the complex-valued steering matrix into a real-valued one for spherical arrays [28]. But this transformation method only suitable for an open sphere. Carlin et al. constructed a real-valued DOA estimation model for any array structure [29]. However, they just combined all the real part and imaginary part directly and this method cannot reduce the computational cost. Moreover, this method destroyed the joint sparsity between the real part and imaginary part of sparse signals. Another method retains the appropriate basis functions while pruning superfluous basis functions from the steering matrix [30, 31]. This basis-pruned approach can achieve similar performance to that of the original algorithm without pruning. However, it either needs an appropriate threshold value or needs to judge basis function sequentially.

Compared with ULAs, spherical arrays have 3-D symmetric structure and can capture high order sound field information [32-35]. Therefore, they have received considerable attention and widely used in source localization [34, 35]. In this paper, we construct a real-valued off-grid model in the real spherical harmonics domain and propose a real-valued SBL algorithm to estimate off-grid DOAs. The matching matrix including angular differences is constructed by computing partial derivatives of the steering matrix with respect to azimuths and elevations. Meanwhile we transform it to a real-valued matrix by a unitary transformation according to its conjugate property. Then we construct a conjugate augmented output matrix and separate its real part and imaginary part by another unitary transformation to build a real-valued off-grid model. Variational sparse Bayesian learning (VSBL) is used to model the joint sparsity between real part and imaginary part of signals. The hyper-parameters are estimated according to their posterior distributions instead of point estimates in VSBL. In order to further reduce computations, an improved real-valued algorithm combining a projection-based basis selection SBL with least squares (PSBL-LS) method is proposed to estimate off-grid DOAs. It uses the potential basis functions selected from the matching matrix to learning the posterior distribution of sparse signals. Moreover, the angular differences are estimated by least squares method based on the selected basis functions. The number of selected basis functions is much smaller than the number of sampling grids, so PSBL-LS algorithm can reduce computations greatly. Simulations show our proposed method can achieve low complexity and simultaneously maintain good accuracy.

We use bold-face letters for vectors and matrices and lowercase letters for scalars. $\mathbf{x}^*$, $\mathbf{x}^{\mathrm{T}}$, and $\mathbf{x}^{\mathrm{H}}$ denote the complex conjugate, transpose, and conjugate transpose of a vector, respectively. $\|\cdot\|_2$ denotes the l_2-norm, $\|\cdot\|_{\mathrm{F}}$ denotes Frobenious norm, and $|\lambda|$ denotes the absolute value of λ. tr{$\mathbf{A}$} is trace of a matrix, respectively. $\mathbf{A}_{i,:}$, $\mathbf{A}_{:,j}$, and $\mathbf{A}_{i,j}$ are the ith row, the jth column, and the (i, j)th entry of a matrix $\mathbf{A}$, respectively. diag($\mathbf{A}$) denotes a column vector composed of the diagonal elements of a matrix $\mathbf{A}$, vec($\mathbf{A}$) denotes the vectorization operator that turns a matrix $\mathbf{A}$ into a vector by concatenating all the columns, and diag($\mathbf{x}$) is a diagonal matrix with $\mathbf{x}$ being its diagonal elements. Re($\mathbf{x}$) and Im($\mathbf{x}$) represent the real part and imaginary part of a complex vector $\mathbf{x}$, respectively. $\mathbf{x}\odot\mathbf{y}$ is the Hadamard product of $\mathbf{x}$ and $\mathbf{y}$. $|\mathbf{x}|$ returns a vector consisting the absolute value of each element in $\mathbf{x}$. $\mathbf{I}_n$ is an $n \times n$ identity matrix and $\mathbf{J}_n$ stands for an $n \times n$ matrix with ones on its anti-diagonal positions and zeroes elsewhere. $\Gamma(\cdot|b, c)$ denotes the Gamma distribution with the parameters b and c. $\mathcal{RN}(\mu, \mathbf{\Sigma})$ means the probability density function (pdf) of a real-valued Gaussian distributed random variable with mean $\boldsymbol{\mu}$ and covariance $\mathbf{\Sigma}$. var{$\mathbf{x}$} returns the variance of the vector $\mathbf{x}$. $\mathbf{\Gamma}^u$ denotes an index set and $\emptyset$ denotes an empty set. $\mathbf{A}_{\mathbf{\Gamma}^u}$, $\mathbf{F}_{\mathbf{\Gamma}^u}$, $\mathbf{C}_{\mathbf{\Gamma}^u}$, and $\mathbf{G}_{\mathbf{\Gamma}^u}$ are matrices obtained from $\mathbf{A}_r$, $\mathbf{F}_r$, $\mathbf{C}_r$, and $\mathbf{G}_r$ by retaining their columns indexed by $\mathbf{\Gamma}^u$, respectively. $\mathbf{\Sigma}_{\mathbf{\Gamma}^u}$, $\mathbf{U}_{\mathbf{\Gamma}^u}$, and $\langle\boldsymbol{\alpha}_{\mathbf{\Gamma}^u}\rangle_q$ denote learning results based on the index set $\mathbf{\Gamma}^u$, $\boldsymbol{\beta}_{1\mathbf{\Gamma}^\eta}$ and $\boldsymbol{\beta}_{2\mathbf{\Gamma}^\eta}$ denote learning results based on the support set $\mathbf{\Gamma}^\eta$. dim($\mathbf{\Gamma}^u$) denotes the dimension of $\mathbf{\Gamma}^u$.

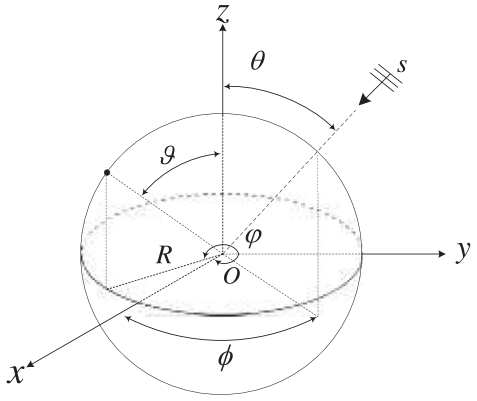

Fig. 1. Spherical coordinate system for localization.

2. Off-grid DOA estimation model in real spherical harmonics domain

We consider a spherical array made of L identical isotropic elements with radius R. The position of the lth sensor can be described as $\mathbf{R}_l = (R\cos\varphi_l \sin\vartheta_l, R\sin\varphi_l \sin\vartheta_l, R\cos\vartheta_l)^{\mathrm{T}}$ in the Cartesian coordinate from Fig. 1, where ϑ_l and φ_l represent the elevation and azimuth of the sensor, respectively. Assuming D narrowband far-field signals with the wavenumber k impinge on the array from $\Phi_d = (\theta_d, \phi_d)$, where θ_d and ϕ_d are the elevation and azimuth of the dth source signal, respectively. The sensors output can be described as

$$\mathbf{x}(t) = \mathbf{A}\mathbf{s}(t) + \mathbf{v}(t), \qquad t = 1, \ \ldots \ , T \tag{1}$$

where $\mathbf{x}(t) = [x_1(t), ..., x_L(t)]^{\mathrm{T}}$ is the output vector, $\mathbf{s}(t) = [s_1(t), ..., s_D(t)]^{\mathrm{T}}$ is the signal vector, $\mathbf{A} = [\mathbf{a}(\Phi_1), ..., \mathbf{a}(\Phi_D)]$ is the steering matrix consisting of D steering vectors $\mathbf{a}(\Phi_d)$, and $\mathbf{v}(t) = [v_1(t), ..., v_L(t)]^T$ is an additive white Gaussian noise vector.

The lth element of the steering vector $\mathbf{a}(\Phi_d)$ is $a_l(\Phi_d) = e^{-j\mathbf{k}_d^{\mathrm{T}}\mathbf{R}_l}$, where $\mathbf{k}_d = -k(\sin\theta_d\cos\phi_d, \sin\theta_d\sin\phi_d, \cos\theta_d)^{\mathrm{T}}$. According to [36], $a_l(\Phi_d)$ can be represented in spherical harmonics as

$$a_l(\Phi_d) = \sum_{n=0}^{N}\sum_{m=-n}^{n} b_n(kR)[Y_n^m(\Phi_d)]^* Y_n^m(\Omega_l), \tag{2}$$

where $\Omega_l = (\vartheta_l, \varphi_l)$ is the spherical angle of the lth sensor position, N is the maximum spherical harmonics order, $b_n(kR)$ is the far-field mode strength with

$$b_n(kR) = \begin{cases} 4\pi i^n j_n(kR), & \text{open sphere} \\ 4\pi i^n (j_n(kR) - \dfrac{j'_n(kR)}{h'_n(kR)} h_n(kR)), & \text{rigid sphere} \end{cases} \tag{3}$$

where j_n stands for spherical Bessel function, h_n is spherical Hankel function, j'_n and h'_n are derivatives of j_n and h_n, respectively.

$Y_n^m(\theta,\phi)$ is the spherical harmonic with order n and degree m defined as

$$Y_n^m(\theta,\phi)=\sqrt{\frac{2n+1}{4\pi}\frac{(n-m)!}{(n+m)!}}P_n^m(cos\theta)e^{im\phi}, \tag{4}$$

where $0\le n\le N, -n\le m\le n$, and $P_n^m(\cos\theta)$ is the associated Legendre polynomial [33]. So the steering matrix can be described as

$$\mathbf{A}=\mathbf{Y}(\mathbf{\Omega})\mathbf{B}(k)\mathbf{Y}^{\mathrm{H}}(\mathbf{\Phi}), \tag{5}$$

where $\mathbf{Y}(\mathbf{\Omega})$ is an $L\times J$ spherical harmonic matrix with $J=(N+1)^2$ whose lth row is given as

$$\mathbf{y}(\Omega_l)=[Y_0^0(\Omega_l),Y_1^{-1}(\Omega_l),Y_1^0(\Omega_l),Y_1^1(\Omega_l),...,Y_N^N(\Omega_l)]. \tag{6}$$

The $D\times J$ matrix $\mathbf{Y}(\mathbf{\Phi})$ can be expressed as the same form. $\mathbf{B}(k)=diag\{b_0(kR),b_1(kR),b_1(kR),b_1(kR),...,b_N(kR)\}$ is a $J\times J$ far-field mode strength matrix.

The spherical Fourier transform $\mathbf{x}_{nm}(t)$ of a spatial domain signal $\mathbf{x}(t)$ involves an integral over all angles, however it can be approximated for a discretely sampled sound field using the expression [34]

$$x_{nm}(t)\cong\sum_{l=1}^{L}c_l x_l(t)[Y_n^m(\Omega_l)]^* \tag{7}$$

where c_l is the sampling weight. Rewriting (7) in a matrix form, we have

$$\mathbf{x_{nm}}(t)=\mathbf{Y}^{\mathrm{H}}(\mathbf{\Omega})\mathbf{\Gamma}\mathbf{x}(t), \tag{8}$$

where $\mathbf{x_{nm}}(t)=[x_{00},x_{1(-1)},x_{10},x_{11},...,x_{NN}]^{\mathrm{T}}$ and $\mathbf{\Gamma}=\mathrm{diag}(c_1,...,c_L)^{\mathrm{T}}$. Under the approximation of (7), spherical harmonics satisfy the following orthogonality

$$\mathbf{Y}^{\mathrm{H}}(\mathbf{\Omega})\mathbf{\Gamma}\mathbf{Y}(\mathbf{\Omega})=\mathbf{I}_J. \tag{9}$$

Following the convention in [37], we multiply both sides of (1) by $\mathbf{W}=\mathbf{B}^{-1}(k)\mathbf{Y}^{\mathrm{H}}(\mathbf{\Omega})\mathbf{\Gamma}$ that is known for a given array geometry and utilize these relations in (5), (8), and (9), the model in the complex spherical harmonics domain becomes

$$\mathbf{x}_c(t)=\mathbf{A}_c\mathbf{s}(t)+\mathbf{v}_c(t), \tag{10}$$

where $\mathbf{x}_c(t)=\mathbf{B}^{-1}(k)\mathbf{x_{nm}}(t)$, $\mathbf{A}_c=\mathbf{Y}^{\mathrm{H}}(\mathbf{\Phi})$, and $\mathbf{v}_c(t)=\mathbf{W}\mathbf{v}(t)$.

Following the concept of sparse reconstruction, the elevation and azimuth are discretized into $H_1\gg D$ and $H_2\gg D$ possible grids, respectively. That is to say, the whole angular space is divided into $H=H_1H_2$ grids noted as $\tilde{\mathbf{\Phi}}=\{\tilde{\Phi}_1,\ldots,\tilde{\Phi}_H\}$ with $\tilde{\Phi}_h=(\tilde{\theta}_h,\tilde{\phi}_h)$, $h=1,\ldots,H$. The measurement matrix is constructed on these discretized spatial angles as follows

$$\bar{\mathbf{A}}_c=[\mathbf{a}_c(\tilde{\Phi}_1),\ldots,\mathbf{a}_c(\tilde{\Phi}_H)], \tag{11}$$

where the hth column of measurement matrix $\bar{\mathbf{A}}_c$ is $\mathbf{a}_c(\tilde{\Phi}_h)=[a_0^0(\tilde{\Phi}_h),a_1^{-1}(\tilde{\Phi}_h),a_1^0(\tilde{\Phi}_h),a_1^1(\tilde{\Phi}_h),\ldots,a_N^N(\tilde{\Phi}_h)]^{\mathrm{T}}$, and $a_n^m(\tilde{\Phi}_h)=a_n^m(\tilde{\theta}_h,\tilde{\phi}_h)=\sqrt{\frac{2n+1}{4\pi}\frac{(n-m)!}{(n+m)!}}P_n^m(cos\tilde{\theta}_h)e^{im\tilde{\phi}_h}$ where $0\le n\le N, -n\le m\le n$. Our main purpose is to find a support set $\mathbf{\Gamma}\subset\{1,...,H\}$ that records the indices of the nonzero entries of $\mathbf{s}(t)$.

Suppose that the dth source signal impinges on the sensors from the angle Φ_d which is not contained in the predefined angular grids. That is to say, $\Phi_d\notin\tilde{\mathbf{\Phi}}$ and $\tilde{\Phi}_{h_d}\in\tilde{\mathbf{\Phi}}$ is the nearest grid to Φ_d, where $d\in\{1,...,D\}$ and $h_d\in\{1,...,H\}$. In such a case, the corresponding matching vector $\mathbf{a}_c(\Phi_d)$ can be approximated by the multivariable Taylor expansion

$$\mathbf{a}_c(\Phi_d)\approx\mathbf{a}_c(\tilde{\Phi}_{h_d})+\mathbf{f}(\tilde{\Phi}_{h_d})(\theta_d-\tilde{\theta}_{h_d})+\mathbf{c}(\tilde{\Phi}_{h_d})(\phi_d-\tilde{\phi}_{h_d}), \tag{12}$$

where $\mathbf{f}(\tilde{\Phi}_{h_d})=\partial\mathbf{a}_c(\tilde{\Phi}_{h_d})/\partial\tilde{\theta}_{h_d}$ and $\mathbf{c}(\tilde{\Phi}_{h_d})=\partial\mathbf{a}_c(\tilde{\Phi}_{h_d})/\partial\tilde{\phi}_{h_d}$. The elements in $\mathbf{f}(\tilde{\Phi}_{h_d})$ can be represented as

$$f_n^m(\tilde{\Phi}_{h_d})=\sqrt{\frac{2n+1}{4\pi}\frac{(n-m)!}{(n+m)!}}\frac{\partial P_n^m(cos\tilde{\theta}_{h_d})}{\partial\tilde{\theta}_{h_d}}e^{im\tilde{\phi}_{h_d}}, \tag{13}$$

where $\frac{\partial P_n^m(cos\tilde{\theta}_{h_d})}{\partial\tilde{\theta}_{h_d}}=\frac{(n-m+1)P_{n+1}^m(\cos\tilde{\theta}_{h_d})-(n+1)\cos\tilde{\theta}_{h_d}P_n^m(\cos\tilde{\theta}_{h_d})}{\sin\tilde{\theta}_{h_d}}$. The elements in $\mathbf{c}(\tilde{\Phi}_{h_d})$ can be represented as

$$c_n^m(\tilde{\Phi}_{h_d})=im\sqrt{\frac{2n+1}{4\pi}\frac{(n-m)!}{(n+m)!}}P_n^m(cos\tilde{\theta}_{h_d})e^{im\tilde{\phi}_{h_d}}. \tag{14}$$

We define two $J\times H$ matrices $\mathbf{F}=[\mathbf{f}(\tilde{\Phi}_1),...,\mathbf{f}(\tilde{\Phi}_H)]$ and $\mathbf{C}=[\mathbf{c}(\tilde{\Phi}_1),...,\mathbf{c}(\tilde{\Phi}_H)]$ for all H sampling grids, and

$$\mathbf{G}(\boldsymbol{\beta}_1,\boldsymbol{\beta}_2)=\bar{\mathbf{A}}_c+\mathbf{F}\mathrm{diag}(\boldsymbol{\beta}_1)+\mathbf{C}\mathrm{diag}(\boldsymbol{\beta}_2), \tag{15}$$

is called the matching matrix whose elements are $g_n^m(\beta_{1h},\beta_{2h})=a_n^m(\tilde{\Phi}_h)+f_n^m(\tilde{\Phi}_h)\beta_{1h}+c_n^m(\tilde{\Phi}_h)\beta_{2h}$. For $d=1,...,D$, $\beta_{1h_d}=\theta_d-\tilde{\theta}_{h_d}$, $\beta_{2h_d}=\phi_d-\tilde{\phi}_{h_d}$, the rest elements of $\boldsymbol{\beta}_1$ and $\boldsymbol{\beta}_2$ are equal to 0, $\boldsymbol{\beta}_1=[\beta_{11},...,\beta_{1H}]^{\mathrm{T}}$, and $\boldsymbol{\beta}_2=[\beta_{21},...,\beta_{2H}]^{\mathrm{T}}$. The 2-D off-grid DOA observation model corresponding to (10) can be formulated as

$$\mathbf{x}_c(t)=\mathbf{G}\bar{\mathbf{s}}(t)+\mathbf{v}_c(t), \tag{16}$$

where $\mathbf{G}$ represents $\mathbf{G}(\boldsymbol{\beta}_1,\boldsymbol{\beta}_2)$ for simplicity and the columns of $\mathbf{G}$ are called basis functions. $\bar{\mathbf{s}}(t)=[\bar{s}_1(t),...,\bar{s}_H(t)]^{\mathrm{T}}$ is the sparse signal vector with $\bar{s}_{h_d}(t)=s_d(t)$ and the rest elements of $\bar{\mathbf{s}}(t)$ being zeroes. From (16), we can see only D basis functions in $\mathbf{G}$ corresponding to D nonzero signals in $\bar{\mathbf{s}}(t)$ are effective and the rest basis functions have no contributions to the observation data in the model.

To apply real-valued sparse Bayesian inference to estimate DOAs efficiently, we manage to find out a method to transform the model (16) into a real-valued model. According to [38], the associated Legendre function has the relation as $P_n^{-m}(\theta)=(-1)^m\frac{(n-m)!}{(n+m)!}P_n^m(\theta)$. Substituting this property into (4), (13), and (14), we can get $a_n^{-m}(\tilde{\Phi}_h)=(-1)^m[a_n^m(\tilde{\Phi}_h)]^*$, $f_n^{-m}(\tilde{\Phi}_h)=(-1)^m[f_n^m(\tilde{\Phi}_h)]^*$, and $c_n^{-m}(\tilde{\Phi}_h)=(-1)^m[c_n^m(\tilde{\Phi}_h)]^*$. Therefore, according to (15), it is easy to get

$$g_n^{-m}(\beta_{1h},\beta_{2h})=(-1)^m[g_n^m(\beta_{1h},\beta_{2h})]^*. \tag{17}$$

Inspired by this property, we divide the complex-valued matching matrix $\mathbf{G}$ into $N+1$ blocks as $\mathbf{G}=[\underbrace{\mathbf{g}_0^0}_{\mathbf{G}_0},\underbrace{\mathbf{g}_1^{-1},\mathbf{g}_1^0,\mathbf{g}_1^1}_{\mathbf{G}_1},...,\underbrace{\mathbf{g}_N^{-N},...,\mathbf{g}_N^N}_{\mathbf{G}_N}]^{\mathrm{T}}=[\mathbf{G}_0,...,\mathbf{G}_N]^{\mathrm{T}}$, where $\mathbf{g}_n^m=[g_n^m(\beta_{11},\beta_{21}),...,g_n^m(\beta_{1H},\beta_{2H})]^{\mathrm{T}}$. Then, we manage to transform $\mathbf{G}$ into a real-valued matrix based on the real spherical harmonics according to its block structure. For each block $\mathbf{G}_n$, a unitary matrix is constructed as follows:

$$\mathbf{Q}_n=\frac{1}{\sqrt{2}}\begin{bmatrix}i\mathbf{Z}_n & \mathbf{0}_n & -i\mathbf{J}_n\\ \mathbf{0}_n^T & \sqrt{2} & \mathbf{0}_n^T\\ \mathbf{J}_n\mathbf{Z}_n & \mathbf{0}_n & \mathbf{I}_n\end{bmatrix}, \tag{18}$$

where $n\ge1$, $\mathbf{0}_n$ represents a column vector containing n zeroes, $\mathbf{Z}_n$ is an $n\times n$ diagonal matrix as $\mathbf{Z}_n=\mathrm{diag}\{(-1)^n,...,(-1)^1\}$. When $n=0$, $\mathbf{Q}_0=1$. It is easy to check $\bar{\mathbf{G}}_n^{\mathrm{T}}=\mathbf{Q}_n\mathbf{G}_n^{\mathrm{T}}$ is a real-valued matrix. Then a block diagonal matrix composed of $\mathbf{Q}_n$ is constructed

$$\mathbf{Q}=\mathrm{blk}diag\{\mathbf{Q}_0,\cdots,\mathbf{Q}_N\}, \tag{19}$$

which is also a unitary matrix. As a result, a real-valued matrix is built by the unitary transformation $\mathbf{G}_r=\mathbf{Q}\mathbf{G}=[\bar{\mathbf{G}}_0,...,\bar{\mathbf{G}}_N]^{\mathrm{T}}$. The elements of $\mathbf{G}_r$ can be represented as

$$\bar{g}_n^m(\beta_{1h},\beta_{2h})=\begin{cases}\sqrt{2}Im\{g_n^{|m|}(\beta_{1h},\beta_{2h})\}, & m<0\\ g_n^0(\beta_{1h},\beta_{2h}), & m=0\\ \sqrt{2}Re\{g_n^m(\beta_{1h},\beta_{2h})\}, & m>0\end{cases}, \tag{20}$$

which are based on the real spherical harmonic function $\bar{a}_n^m(\tilde{\theta}_h, \tilde{\phi}_h)$

$$\bar{a}_n^m(\tilde{\theta}_h, \tilde{\phi}_h) = \begin{cases} \sqrt{\frac{2n+1}{2\pi}\frac{(n-|m|)!}{(n+|m|)!}} P_n^{|m|}(cos\tilde{\theta}_h)\sin|m|\tilde{\phi}_h, & m<0 \\ \sqrt{\frac{2n+1}{4\pi}} P_n^0(cos\tilde{\theta}_h), & m=0 \\ \sqrt{\frac{2n+1}{2\pi}\frac{(n-m)!}{(n+m)!}} P_n^m(cos\tilde{\theta}_h)\cos m\tilde{\phi}_h, & m>0 \end{cases} . \tag{21}$$

In detail, $\bar{g}_n^m(\beta_{1h}, \beta_{2h})$ can be written as $\bar{g}_n^m(\beta_{1h}, \beta_{2h}) = \bar{a}_n^m(\tilde{\Phi}_h) + \frac{\partial \bar{a}_n^m(\tilde{\Phi}_h)}{\partial \tilde{\theta}_h}\beta_{1h} + \frac{\partial \bar{a}_n^m(\tilde{\Phi}_h)}{\partial \tilde{\phi}_h}\beta_{2h}$. Meanwhile $\mathbf{G}_r = \mathbf{A}_r + \mathbf{F}_r\mathrm{diag}(\boldsymbol{\beta}_1) + \mathbf{C}_r\mathrm{diag}(\boldsymbol{\beta}_2)$ with $\mathbf{A}_r = \mathbf{Q}\bar{\mathbf{A}}_c$, $\mathbf{F}_r = \mathbf{QF}$, and $\mathbf{C}_r = \mathbf{QC}$. So, the model in (16) can be transformed into the real spherical harmonics domain through multiplying both sides of (16) by a block diagonal matrix $\mathbf{Q}$

$$\mathbf{Q}\mathbf{x}_c(t) = \mathbf{G}_r\bar{\mathbf{s}}(t) + \mathbf{Q}\mathbf{v}_c(t). \tag{22}$$

From (22), we can see that only $\mathbf{G}_r$ is real and the other elements are still complex. In order to transform (22) into a completely real-valued model, we devise a conjugate augmented matrix $\mathbf{x}_a(t)$ of the output in (22) and let its each row satisfy the conjugate symmetric property. So the conjugate augmented matrix $\mathbf{x}_a(t)$ is designed as $\mathbf{x}_a(t) = [\mathbf{Q}\mathbf{x}_c(t), \mathbf{Q}^*\mathbf{x}_c^*(t)]$. A unitary matrix is defined as

$$\bar{\mathbf{Q}} = \frac{1}{\sqrt{2}}\begin{bmatrix} 1 & -i \\ 1 & i \end{bmatrix}. \tag{23}$$

Multiplying $\mathbf{x}_a(t)$ by $\bar{\mathbf{Q}}$ on the right side, we can get

$$\mathbf{x}_a(t)\bar{\mathbf{Q}} = [\mathbf{Q}\mathbf{x}_c(t), \mathbf{Q}^*\mathbf{x}_c^*(t)]\bar{\mathbf{Q}} = \sqrt{2}[Re(\mathbf{Q}\mathbf{x}_c(t)), Im(\mathbf{Q}\mathbf{x}_c(t))] \tag{24}$$

Substituting (22) into (24), we can get

$$\begin{aligned} \mathbf{x}_a(t)\bar{\mathbf{Q}} &= [\mathbf{G}_r\bar{\mathbf{s}}(t) + \mathbf{Q}\mathbf{v}_c(t), \mathbf{G}_r^*\bar{\mathbf{s}}^*(t) + \mathbf{Q}^*\mathbf{v}_c^*(t)]\bar{\mathbf{Q}} \\ &= [\mathbf{G}_r\bar{\mathbf{s}}(t), \mathbf{G}_r^*\bar{\mathbf{s}}^*(t)]\bar{\mathbf{Q}} + [\mathbf{Q}\mathbf{v}_c(t), \mathbf{Q}^*\mathbf{v}_c^*(t)]\bar{\mathbf{Q}} \\ &= \sqrt{2}\mathbf{G}_r[Re(\bar{\mathbf{s}}(t)), Im(\bar{\mathbf{s}}(t))] + \sqrt{2}[Re(\mathbf{Q}\mathbf{v}_c(t)), Im(\mathbf{Q}\mathbf{v}_c(t))]. \end{aligned} \tag{25}$$

At last, according to (24) and (25), a completely real-valued model based on the real spherical harmonics is gotten as

$$\bar{\mathbf{X}}_r(t) = \mathbf{G}_r\bar{\mathbf{S}}_r(t) + \bar{\mathbf{V}}_r(t), \tag{26}$$

where $\bar{\mathbf{X}}_r(t) = [Re(\mathbf{Q}\mathbf{x}_c(t)), Im(\mathbf{Q}\mathbf{x}_c(t))]$, $\bar{\mathbf{S}}_r(t) = [Re(\bar{\mathbf{s}}(t)), Im(\bar{\mathbf{s}}(t))]$, and $\bar{\mathbf{V}}_r(t) = [Re(\mathbf{Q}\mathbf{v}_c(t)), Im(\mathbf{Q}\mathbf{v}_c(t))]$. From (26), we know $\bar{\mathbf{S}}_r(t)$ is composed of only D rows being non-zero. Angular differences $\boldsymbol{\beta}_1$ and $\boldsymbol{\beta}_2$ have the same sparsity as $\bar{\mathbf{S}}_r(t)$ and are responsible for reducing the grid mismatch.

3. The proposed PSBL-LS method

DOA estimation under the off-grid model is not only to reconstruct the sparse signal $\bar{\mathbf{S}}_r(t)$ but also to estimate the angular differences $\boldsymbol{\beta}_1$ and $\boldsymbol{\beta}_2$. In this section, we formulate the problem from a real-valued sparse Bayesian perspective and adopt two steps to jointly estimate $\bar{\mathbf{S}}_r(t)$, $\boldsymbol{\beta}_1$, and $\boldsymbol{\beta}_2$. In the first step, the variational sparse Bayesian inference is used to approximate the posterior of sparse signals $\bar{\mathbf{S}}_r(t)$ under the assumption that the angular differences $\boldsymbol{\beta}_1$ and $\boldsymbol{\beta}_2$ are known from the previous iteration. In the second step, we adopt an LS method to estimate the angular differences.

For better performance, we employ the multiple measurement vectors (MMV) and the off-grid DOA estimation model in (26) becomes

$$\mathbf{X}_r = \mathbf{G}_r\mathbf{S}_r + \mathbf{V}_r. \tag{27}$$

where $\mathbf{X}_r = [\bar{\mathbf{X}}_r(1), ..., \bar{\mathbf{X}}_r(T)] = [\mathbf{x}_r(1), ..., \mathbf{x}_r(2T)]$, $\mathbf{S}_r = [\bar{\mathbf{S}}_r(1), ..., \bar{\mathbf{S}}_r(T)] = [\mathbf{s}_r(1), ..., \mathbf{s}_r(2T)]$ and $\mathbf{V}_r = [\bar{\mathbf{V}}_r(1), ..., \bar{\mathbf{V}}_r(T)] = [\mathbf{v}_r(1), ..., \mathbf{v}_r(2T)]$. We model $\mathbf{S}_r$ as a hidden variable and assume the angular differences $\boldsymbol{\beta}_1$ and $\boldsymbol{\beta}_2$ are known from the previous iteration. A two-level hierarchical prior is imposed on the sparse signals $\mathbf{S}_r$ with elements $\mathbf{s}_r(\tau)$, $\tau = 1, ..., 2T$

$$p(\mathbf{S}_r|\boldsymbol{\alpha}) = \prod_{\tau=1}^{2T} \mathcal{RN}(\mathbf{s}_r(\tau)|0, \boldsymbol{\Lambda}^{-1}), \tag{28}$$

and

$$p(\boldsymbol{\alpha}) = \prod_{h=1}^{H} \Gamma(\alpha_h|b^{(\alpha)}, c^{(\alpha)}), \tag{29}$$

where $\boldsymbol{\Lambda} = \mathrm{diag}(\boldsymbol{\alpha})$, $\boldsymbol{\alpha} = [\alpha_1, ..., \alpha_H]^{\mathrm{T}}$. The pdf of the noise vector is assumed as Gaussian with zero-mean and the variance parameter equal to γ^{-1}

$$p(\mathbf{V}_r|\gamma) = \prod_{\tau=1}^{2T} \mathcal{RN}(\mathbf{v}_r(\tau)|0, \gamma^{-1}\mathbf{I}_J) \ , \tag{30}$$

with

$$p(\gamma) = \Gamma(\gamma|b^{(\gamma)}, c^{(\gamma)}), \tag{31}$$

Based on (27) and (30), the distribution of the observations is

$$p(\mathbf{X}_r|\mathbf{S}_r, \gamma) = \prod_{\tau=1}^{2T} \mathcal{RN}(\mathbf{x}_r(\tau)|\mathbf{G}_r\mathbf{s}_r(\tau), \gamma^{-1}\mathbf{I}_J). \tag{32}$$

The variational solution to SBL is obtained by minimizing the Kullback–Leibler (KL) divergence which measures the difference of the probability mass between the approximate posterior distribution $q(\mathbf{S}_r, \boldsymbol{\alpha}, \gamma) = q(\mathbf{S}_r)q(\boldsymbol{\alpha})q(\gamma)$ and its posterior distribution $p(\mathbf{S}_r, \boldsymbol{\alpha}, \gamma|\mathbf{X}_r)$. Since $p(\mathbf{S}_r, \boldsymbol{\alpha}, \gamma|\mathbf{X}_r)$ is usually intractable, calculating $p(\mathbf{S}_r, \boldsymbol{\alpha}, \gamma|\mathbf{X}_r)$ is equivalent to calculate the joint pdf $p(\mathbf{S}_r, \mathbf{X}_r, \boldsymbol{\alpha}, \gamma) = p(\mathbf{S}_r, \boldsymbol{\alpha}, \gamma|\mathbf{X}_r)p(\mathbf{X}_r)$ because $p(\mathbf{X}_r)$ is independent of the parameters. Therefore, the cost function in practice is given by

$$\mathrm{C_{KL}} = \left\langle \ln \frac{q(\mathbf{S}_r, \boldsymbol{\alpha}, \gamma)}{p(\mathbf{S}_r, \mathbf{X}_r, \boldsymbol{\alpha}, \gamma)} \right\rangle_q = \left\langle \ln \frac{q(\mathbf{S}_r)q(\boldsymbol{\alpha})q(\gamma)}{p(\mathbf{X}_r|\mathbf{S}_r, \gamma)p(\mathbf{S}_r|\boldsymbol{\alpha})p(\boldsymbol{\alpha})p(\gamma)} \right\rangle_q, \tag{33}$$

where $\langle\mathbf{S}_r\rangle_q$ denotes the expectation of $\mathbf{S}_r$ under its distribution $q(\mathbf{S}_r)$. The cost function can be minimized via variational EM strategy [39, 40].

In the variational E-step, $q(\mathbf{S}_r)$ is updated according to $q(\mathbf{S}_r) \propto exp(\langle \ln p(\mathbf{X}_r, \mathbf{S}_r|\boldsymbol{\alpha}, \gamma)\rangle_q)$. According to the distributions $p(\mathbf{X}_r|\mathbf{S}_r, \gamma)$ and $p(\mathbf{S}_r|\boldsymbol{\alpha})$, the joint distribution can be described as $p(\mathbf{X}_r, \mathbf{S}_r|\boldsymbol{\alpha}, \gamma) = p(\mathbf{X}_r|\mathbf{S}_r, \gamma)p(\mathbf{S}_r|\boldsymbol{\alpha})$. Therefore, we have

$$\begin{aligned} \ln q(\mathbf{s}_r(\tau)) = &-\frac{1}{2}\mathbf{s}_r^{\mathrm{T}}(\tau)\left(\langle\gamma\rangle_q\mathbf{G}_r^{\mathrm{T}}\mathbf{G}_r + \boldsymbol{\Lambda}\right)\mathbf{s}_r(\tau) \\ &+ \langle\gamma\rangle_q\mathbf{s}_r^{\mathrm{T}}(\tau)\mathbf{G}_r^{\mathrm{T}}\mathbf{x}_r(\tau) + C_1, \end{aligned} \tag{34}$$

where C_1 is a constant. Notice that (34) is the logarithm of a Gaussian distribution with covariance matrix $\boldsymbol{\Sigma}$ and mean $\mathbf{u}(\tau)$ given by

$$\boldsymbol{\Sigma} = \left(\langle\gamma\rangle_q\mathbf{G}_r^{\mathrm{T}}\mathbf{G}_r + \langle\boldsymbol{\Lambda}\rangle_q\right)^{-1}, \tag{35}$$

$$\mathbf{u}(\tau) = \langle\gamma\rangle_q\boldsymbol{\Sigma}\mathbf{G}_r^{\mathrm{T}}\mathbf{x}_r(\tau). \tag{36}$$

Therefore, we can get the approximate posterior density for $\mathbf{S}_r$ as

$$q(\mathbf{S}_r) = \prod_{\tau=1}^{2T} \mathcal{RN}(\mathbf{s}_r(\tau)|\mathbf{u}(\tau), \boldsymbol{\Sigma}). \tag{37}$$

In the variational M-step, $q(\boldsymbol{\alpha}, \gamma)$ is updated according to $q(\boldsymbol{\alpha}, \gamma) \propto p(\boldsymbol{\alpha}, \gamma)exp(\langle \ln p(\mathbf{X}_r, \mathbf{S}_r|\boldsymbol{\alpha}, \gamma)\rangle_q)$. Assuming all the parameters in $\boldsymbol{\alpha}$ and γ are mutually independent, the joint prior for $\boldsymbol{\alpha}$ and γ can be expressed as $p(\boldsymbol{\alpha}, \gamma) = p(\gamma)\sum_{j=1}^{H} p(\alpha_j)$. The posterior $q(\boldsymbol{\alpha})$ is

obtained by computing the terms of $\ln\ q(\boldsymbol{\alpha})$ that depends on $\boldsymbol{\alpha}$

$$\ln q(\boldsymbol{\alpha}) = (b^{(\alpha)} - 1 + T)\sum_{h=1}^{H}\ln\alpha_h - \sum_{h=1}^{H}\left(\frac{1}{2}\left\langle \mathbf{S}_{h,:}\mathbf{S}_{h,:}^{\mathrm{T}}\right\rangle_q + c^{(\alpha)}\right)\alpha_h + C_2, \tag{38}$$

where C_2 is a constant. This is the logarithm of the product of H independent Gamma distributions with parameters $\bar{b}^{(\alpha)}$ and $\bar{c}_h^{(\alpha)}$ given by

$$\bar{b}^{(\alpha)} = b^{(\alpha)} + T, \tag{39}$$

$$\bar{c}_h^{(\alpha)} = c^{(\alpha)} + \frac{1}{2}\left\langle \mathbf{S}_{h,:}\mathbf{S}_{h,:}^{\mathrm{T}}\right\rangle_q. \tag{40}$$

Thus, $q(\boldsymbol{\alpha})$ is given by $q(\boldsymbol{\alpha}) = \prod_{h=1}^{H}\Gamma(\alpha_h|\bar{b}^{(\alpha)}, \bar{c}_h^{(\alpha)})$. The average for α_h under its posterior is

$$\langle\alpha_h\rangle_q = \bar{b}^{(\alpha)}/\bar{c}_h^{(\alpha)}. \tag{41}$$

The posterior distribution of the noise inverse variance can be similarly computed as $q(\gamma) = \Gamma(\gamma|\bar{b}^{(\gamma)}, \bar{c}^{(\gamma)})$ with

$$\bar{b}^{(\gamma)} = b^{(\gamma)} + JT, \tag{42}$$

$$\bar{c}^{(\gamma)} = c^{(\gamma)} + \frac{1}{2}\left\langle ||\mathbf{X}_r - \mathbf{G}_r\mathbf{S}_r||_{\mathrm{F}}^2\right\rangle_q. \tag{43}$$

The average for γ under its posterior is

$$\langle\gamma\rangle_q = \bar{b}^{(\gamma)}/\bar{c}^{(\gamma)}. \tag{44}$$

Until now, the process of learning posterior distribution of sparse signals $\mathbf{S}_r$ is finished. Before estimating angular differences $\boldsymbol{\beta}_1$ and $\boldsymbol{\beta}_2$, we calculate the support set $\boldsymbol{\Gamma}^{\eta}$ composed by indices of D maximums in $\langle\boldsymbol{\alpha}\rangle_q$. To estimate $\boldsymbol{\beta}_1$ and $\boldsymbol{\beta}_2$, it is difficult to use variational sparse Bayesian inference to approximate their posterior density functions when the prior distributions of $\boldsymbol{\beta}_1$ and $\boldsymbol{\beta}_2$ are not exponential family [40]. In [23], the angular difference was estimated by a maximum a posteriori (MAP) estimate. An EM algorithm is implemented that treats sparse signal $\mathbf{S}_r$ as a hidden variable. Inspired by this method, we minimize the cost function $E\{||\mathbf{X}_r - [\mathbf{A}_r + \mathbf{F}_r\mathrm{diag}(\boldsymbol{\beta}_1) + \mathbf{C}_r\mathrm{diag}(\boldsymbol{\beta}_2)]\mathbf{S}_r||_{\mathrm{F}}^2\}$ with respect to $\boldsymbol{\beta}_1$ and $\boldsymbol{\beta}_2$ based on the posterior information of $\mathbf{S}_r$, where $E(\cdot)$ denotes an expectation with respect to the posterior of $\mathbf{S}_r$. The detail derivations of updating $\boldsymbol{\beta}_1$ and $\boldsymbol{\beta}_2$ by the EM method are given in Appendix. From Appendix, we can see the update process needs to take derivatives with respect to $\boldsymbol{\beta}_1$ and $\boldsymbol{\beta}_2$. Furthermore, if we do not set any priors for $\boldsymbol{\beta}_1$ and $\boldsymbol{\beta}_2$, we can use maximum likelihood (ML) estimate that maximizing $\ln\{p(\mathbf{X}_r|\mathbf{S}_r, \gamma, \boldsymbol{\beta}_1, \boldsymbol{\beta}_2)\}$ with respect to $\boldsymbol{\beta}_1$ and $\boldsymbol{\beta}_2$ to update them. Maximizing $\ln\{p(\mathbf{X}_r|\mathbf{S}_r, \gamma, \boldsymbol{\beta}_1, \boldsymbol{\beta}_2)\}$ with respect to $\boldsymbol{\beta}_1$ and $\boldsymbol{\beta}_2$ is equal to minimize $||\mathbf{X}_r - [\mathbf{A}_r + \mathbf{F}_r\mathrm{diag}(\boldsymbol{\beta}_1) + \mathbf{C}_r\mathrm{diag}(\boldsymbol{\beta}_2)]\mathbf{S}_r||_{\mathrm{F}}^2$. In the first step, we have gotten the posterior mean $\mathbf{U}$ of $\mathbf{S}_r$. Then we can substitute $\mathbf{U}$ for $\mathbf{S}_r$ based on $\boldsymbol{\Gamma}^{\eta}$ in the cost function and minimize $||\mathbf{X}_r - [\mathbf{A}_{\boldsymbol{\Gamma}^{\eta}} + \mathbf{F}_{\boldsymbol{\Gamma}^{\eta}}\mathrm{diag}(\boldsymbol{\beta}_{1\boldsymbol{\Gamma}^{\eta}}) + \mathbf{C}_{\boldsymbol{\Gamma}^{\eta}}\mathrm{diag}(\boldsymbol{\beta}_{2\boldsymbol{\Gamma}^{\eta}})]\mathbf{U}_{\boldsymbol{\Gamma}^{\eta}}||_{\mathrm{F}}^2$. While updating angular difference $\boldsymbol{\beta}_{1\boldsymbol{\Gamma}^{\eta}}$, we keep the current estimate of $\boldsymbol{\beta}_{2\boldsymbol{\Gamma}^{\eta}}$ fixed. In this case, the problem of updating $\boldsymbol{\beta}_{1\boldsymbol{\Gamma}^{\eta}}$ reduces to:

$$\min_{\boldsymbol{\beta}_{1\boldsymbol{\Gamma}^{\eta}}} ||\mathbf{X}_r - [\mathbf{A}_{\boldsymbol{\Gamma}^{\eta}} + \mathbf{F}_{\boldsymbol{\Gamma}^{\eta}}\mathrm{diag}(\boldsymbol{\beta}_{1\boldsymbol{\Gamma}^{\eta}}) + \mathbf{C}_{\boldsymbol{\Gamma}^{\eta}}\mathrm{diag}(\boldsymbol{\beta}_{2\boldsymbol{\Gamma}^{\eta}})]\mathbf{U}_{\boldsymbol{\Gamma}^{\eta}}||_{\mathrm{F}}^2, \tag{45}$$

where $\mathbf{U}_{\boldsymbol{\Gamma}^{\eta}} = [\mathbf{u}_{\boldsymbol{\Gamma}^{\eta}}(1), ..., \mathbf{u}_{\boldsymbol{\Gamma}^{\eta}}(2T)]$. Instead of taking the derivative to obtain $\boldsymbol{\beta}_{1\boldsymbol{\Gamma}^{\eta}}$, we note that for a single snapshot the problem of (45) is equivalent to the LS problem:

$$\mathbf{x}_r(\tau) - [\mathbf{A}_{\boldsymbol{\Gamma}^{\eta}} + \mathbf{C}_{\boldsymbol{\Gamma}^{\eta}}\mathrm{diag}(\boldsymbol{\beta}_{2\boldsymbol{\Gamma}^{\eta}})]\mathbf{u}_{\boldsymbol{\Gamma}^{\eta}}(\tau) = \mathbf{F}_{\boldsymbol{\Gamma}^{\eta}}\Delta_{\mathbf{u}(\tau)}\boldsymbol{\beta}_{1\boldsymbol{\Gamma}^{\eta}}, \tag{46}$$

where $\Delta_{\mathbf{u}(\tau)} = \mathrm{diag}(\mathbf{u}_{\boldsymbol{\Gamma}^{\eta}}(\tau))$.

For T time snapshots, it is straightforward to vectorize the following $2T$ LS problems:

$$\begin{bmatrix} \mathbf{x}_r(1) - [\mathbf{A}_{\boldsymbol{\Gamma}^{\eta}} + \mathbf{C}_{\boldsymbol{\Gamma}^{\eta}}\mathrm{diag}(\boldsymbol{\beta}_{2\boldsymbol{\Gamma}^{\eta}})]\mathbf{u}_{\boldsymbol{\Gamma}^{\eta}}(1) \\ \vdots \\ \mathbf{x}_r(2T) - [\mathbf{A}_{\boldsymbol{\Gamma}^{\eta}} + \mathbf{C}_{\boldsymbol{\Gamma}^{\eta}}\mathrm{diag}(\boldsymbol{\beta}_{2\boldsymbol{\Gamma}^{\eta}})]\mathbf{u}_{\boldsymbol{\Gamma}^{\eta}}(2T) \end{bmatrix} = \begin{bmatrix} \mathbf{F}_{\boldsymbol{\Gamma}^{\eta}}\Delta_{\mathbf{u}(1)} \\ \vdots \\ \mathbf{F}_{\boldsymbol{\Gamma}^{\eta}}\Delta_{\mathbf{u}(2T)} \end{bmatrix}\boldsymbol{\beta}_{1\boldsymbol{\Gamma}^{\eta}}. \tag{47}$$

Therefore, at each iteration the update for $\boldsymbol{\beta}_{1\boldsymbol{\Gamma}^{\eta}}$ is:

$$\boldsymbol{\beta}_{1\boldsymbol{\Gamma}^{\eta}} = \mathbf{F}_{\Delta_{\mathbf{u}}}^{+}\mathbf{R}_1, \tag{48}$$

where $\mathbf{F}_{\Delta_{\mathbf{u}}} = [\mathbf{F}_{\boldsymbol{\Gamma}^{\eta}}\Delta_{\mathbf{u}(1)}, ..., \mathbf{F}_{\boldsymbol{\Gamma}^{\eta}}\Delta_{\mathbf{u}(2T)}]^{\mathrm{T}}$ and $\mathbf{R}_1 = \mathrm{vec}(\mathbf{X}_r - [\mathbf{A}_{\boldsymbol{\Gamma}^{\eta}} + \mathbf{C}_{\boldsymbol{\Gamma}^{\eta}}\mathrm{diag}(\boldsymbol{\beta}_{2\boldsymbol{\Gamma}^{\eta}})]\mathbf{U}_{\boldsymbol{\Gamma}^{\eta}})$. Similarly, at each iteration the update for $\boldsymbol{\beta}_{2\boldsymbol{\Gamma}^{\eta}}$ is:

$$\boldsymbol{\beta}_{2\boldsymbol{\Gamma}^{\eta}} = \mathbf{C}_{\Delta_{\mathbf{u}}}^{+}\mathbf{R}_2, \tag{49}$$

where $\mathbf{C}_{\Delta_{\mathbf{u}}} = [\mathbf{C}_{\boldsymbol{\Gamma}^{\eta}}\Delta_{\mathbf{u}(1)}, ..., \mathbf{C}_{\boldsymbol{\Gamma}^{\eta}}\Delta_{\mathbf{u}(2T)}]^{\mathrm{T}}$ and $\mathbf{R}_2 = \mathrm{vec}(\mathbf{X}_r - [\mathbf{A}_{\boldsymbol{\Gamma}^{\eta}} + \mathbf{F}_{\boldsymbol{\Gamma}^{\eta}}\mathrm{diag}(\boldsymbol{\beta}_{1\boldsymbol{\Gamma}^{\eta}})]\mathbf{U}_{\boldsymbol{\Gamma}^{\eta}})$. Here, we compare the number of real multiplication during the update for $\boldsymbol{\beta}_1$ and $\boldsymbol{\beta}_2$ between LS method and EM method after performing the SVD of the received matrix. The number of real multiplication by LS method is $(4D^3 + 6D^2)J$ while the number of real multiplication by EM method is $(4D^3 + 11D^2)J + 6D^3 + 3D^2$ in each iteration. So the proposed LS method can save computations compared to the EM method. Meanwhile, we compare the estimate accuracy of angular differences $\boldsymbol{\beta}_1$ and $\boldsymbol{\beta}_2$ by LS and EM methods in Fig. 2 and we can see the two methods achieve similar performance.

Since $\boldsymbol{\beta}_1$ and $\boldsymbol{\beta}_2$ are angular differences between directions of arriving signals and nearest sampling grids, so $\beta_{1h} \in [-0.5r, 0.5r]$ and $\beta_{2h} \in [-0.5r, 0.5r]$, r is the grid interval. If $|\beta_{1h}| > 0.5r$, we set $|\beta_{1h}| = 0.5r$. β_2 obeys the same criterion. The successive steps of the proposed algorithm are summarized in Algorithm 1.

In Algorithm 1, the dimension of the matching matrix $\mathbf{G}_r$ is $J \times H$, which can cause high computational complexity with dense sampling grid even in the real-valued model. In order to further reduce computations, the basis-pruned approach was proposed in [30, 31]. First, a small pruning threshold is set for the sparse parameter $\langle\alpha_h\rangle_q^{-1}$. During the iteration learning, when $\langle\alpha_h\rangle_q^{-1}$ is less than the small pruning threshold, the corresponding basis function is removed from the matching matrix $\mathbf{G}_r$. Compared with the basis-pruned approach, [30] also demonstrated we can start with an empty model and add basis function sequentially. Each time a new basis function is tested whether it should be retained or pruned in the model. This is also time-consuming. Motivated by the projection-based basis selection idea [41], we propose a PSBL-LS algorithm to improve the efficiency of Algorithm 1.

Algorithm 2 describes the detailed PSBL-LS algorithm. In each iteration, the matched filter selects L indices as a potential index set $\boldsymbol{\Gamma}^{L}$. To select the most favorable basis index from $\boldsymbol{\Gamma}^{L}$, the PSBL-LS algorithm constructs a union set $\boldsymbol{\Gamma}^{u} = \boldsymbol{\Gamma}^{\eta} \cup \boldsymbol{\Gamma}^{L}$, where $\boldsymbol{\Gamma}^{\eta}$ is the support set of previous iteration and $\boldsymbol{\Gamma}^{\eta} \cap \boldsymbol{\Gamma}^{L} = \emptyset$. Then we learn the posterior variance $\boldsymbol{\Sigma}_{\boldsymbol{\Gamma}^{u}}$, mean $\mathbf{U}_{\boldsymbol{\Gamma}^{u}}$, and hyper-parameters $\langle\boldsymbol{\alpha}_{\boldsymbol{\Gamma}^{u}}\rangle_q$ and $\langle\gamma\rangle_q$ of the sparse signals. After the VSBL converges, we update angular differences $\boldsymbol{\beta}_{1\boldsymbol{\Gamma}^{\eta}}$ and $\boldsymbol{\beta}_{2\boldsymbol{\Gamma}^{\eta}}$ according to the support set $\boldsymbol{\Gamma}^{\eta}$. Last, PSBL-LS algorithm selects the optimal index from $\boldsymbol{\Gamma}^{L}$ according to $\langle\boldsymbol{\alpha}_{\boldsymbol{\Gamma}^{L}}\rangle_q$ to update support set $\boldsymbol{\Gamma}^{\eta}$. The new residual is updated by the posterior mean of the sparse signals.

During the learning process in Algorithm 2, the column of $\mathbf{G}$ becomes $\dim(\boldsymbol{\Gamma}^{u})$ which is much smaller than H in Algorithm 1. So Algorithm 2 reduces computations greatly. When the algorithm converges, the nearest grid to true DOAs are selected from the set $\tilde{\boldsymbol{\Phi}}$ according to $\boldsymbol{\Gamma}^{\eta}$. Finally, the true DOAs are obtained by summing the selected grid and the corresponding differences $\boldsymbol{\beta}_{1\boldsymbol{\Gamma}^{\eta}}$ and $\boldsymbol{\beta}_{2\boldsymbol{\Gamma}^{\eta}}$ in Algorithm 1 and Algorithm 2.

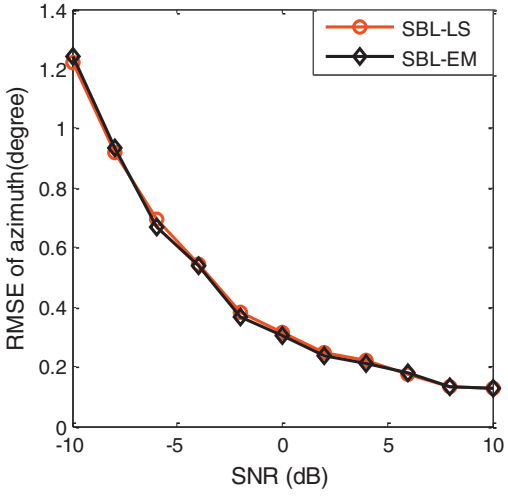

(a) RMSE of azimuth versus SNR

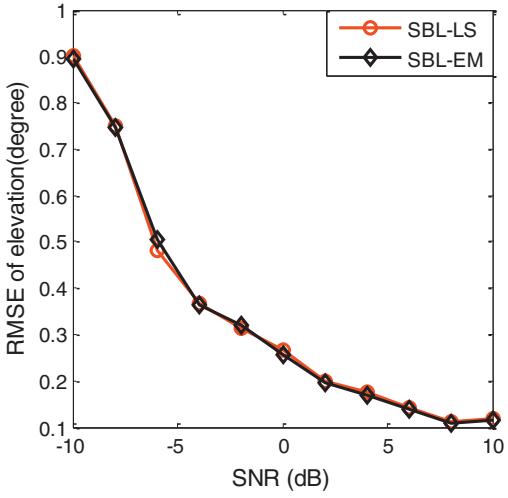

(b) RMSE of elevation versus SNR

Fig. 2. Performance of SBL-EM and SBL-LS methods.

Algorithm 1
SBL-LS algorithm to 2-D off-grid DOA estimation in real spherical harmonics domain.

Initialize the parameters $\langle\boldsymbol{\alpha}\rangle_q$, $\langle\gamma\rangle_q$, $\boldsymbol{\beta}_1$, $\boldsymbol{\beta}_2$, $b^{(\alpha)}$, $c^{(\alpha)}$, $b^{(\gamma)}$, and $c^{(\gamma)}$; set the iteration counter $\eta = 1$.
do
Update $\boldsymbol{\Sigma}$ by (35);
Update $\mathbf{U}$ by (36);
Update $\langle\alpha_h\rangle_q$ by (41);
Update $\langle\gamma\rangle_q$ by (44);
Update $\boldsymbol{\Gamma}^\eta$ by indices corresponding to D maximums in $\langle\boldsymbol{\alpha}\rangle_q$;
Update $\boldsymbol{\beta}_{1\boldsymbol{\Gamma}^\eta}$ and $\boldsymbol{\beta}_{2\boldsymbol{\Gamma}^\eta}$ by (48)–(49);
$\eta \leftarrow \eta + 1$.
while $\sum_{h=1}^{H}(\langle\alpha_h^{new}\rangle_q^{-1} - \langle\alpha_h^{old}\rangle_q^{-1})^2 / \sum_{h=1}^{H}(\langle\alpha_h^{old}\rangle_q^{-1})^2$ and $\eta < \eta_{\max}$

where μ is a user-defined tolerance, $\eta_{\max}$ is a number of the maximum iterations. $\langle\alpha_h^{new}\rangle_q$ denotes the value of $\langle\alpha_h\rangle_q$ in the current iteration and $\langle\alpha_h^{old}\rangle_q$ denotes the value of $\langle\alpha_h\rangle_q$ in the last iteration.

Algorithm 2
PSBL-LS algorithm to 2-D off-grid DOA estimation in real spherical harmonics domain.

Initialize the parameters $\langle\boldsymbol{\alpha}\rangle_q$, $\langle\gamma\rangle_q$, $\boldsymbol{\beta}_1$, $\boldsymbol{\beta}_2$, $b^{(\alpha)}$, $c^{(\alpha)}$, $b^{(\gamma)}$, and $c^{(\gamma)}$; set the iteration counter $\eta = 0$, $\boldsymbol{\Gamma}^0 = \emptyset$, and $\mathbf{R} = \mathbf{X}_r$.
while $\eta \leq D$
$\boldsymbol{\Gamma}^L = \arg\max_{h\notin\boldsymbol{\Gamma}^\eta} L(||\mathbf{G}_{r(:,h)}^{\mathrm{T}}\mathbf{R}||_2)$;
$\boldsymbol{\Gamma}^u = \boldsymbol{\Gamma}^\eta \cup \boldsymbol{\Gamma}^L$;
do
Update $\boldsymbol{\Sigma}_{\boldsymbol{\Gamma}^u}$ by (35);
Update $\mathbf{U}_{\boldsymbol{\Gamma}^u}$ by (36);
Update $\langle\boldsymbol{\alpha}_{\boldsymbol{\Gamma}^u}\rangle_q$ by (41);
Update $\langle\gamma\rangle_q$ by (44);
Update $\boldsymbol{\beta}_{1\boldsymbol{\Gamma}^\eta}$ and $\boldsymbol{\beta}_{2\boldsymbol{\Gamma}^\eta}$ by (48)-(49);
while $\sum_{h\in\boldsymbol{\Gamma}^u}(\langle\alpha_h^{new}\rangle_q^{-1} - \langle\alpha_h^{old}\rangle_q^{-1})^2 / \sum_{h\in\boldsymbol{\Gamma}^u}(\langle\alpha_h^{old}\rangle_q^{-1})^2 > \mu$
If $\eta = D$, **break;**
$\eta = \eta + 1$;
$h_\eta = \underset{h\in\boldsymbol{\Gamma}^L}{\mathrm{argmax}}(\langle\alpha_h\rangle_q)$, $\boldsymbol{\Gamma}^\eta = \boldsymbol{\Gamma}^{\eta-1} \cup h_\eta$;
$\mathbf{R} = \mathbf{X}_r - \mathbf{G}_{\boldsymbol{\Gamma}^\eta}\mathbf{U}_{\boldsymbol{\Gamma}^\eta}$;
End while
where μ is a user-defined tolerance parameter.

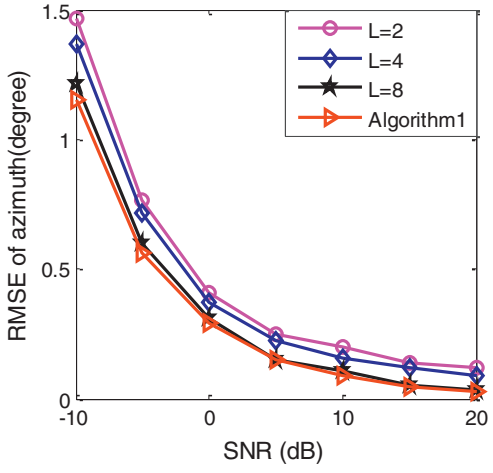

(a) RMSE of azimuth versus SNR

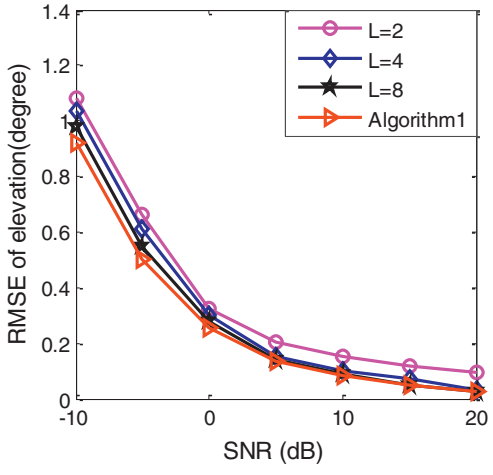

(b) RMSE of elevation versus SNR

Fig. 3. RMSEs of the proposed PSBL-LS with the number of selected potential basis functions L.

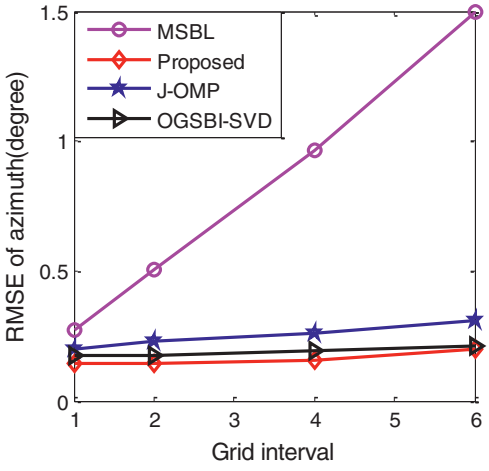

(a) RMSE of azimuth versus grid interval

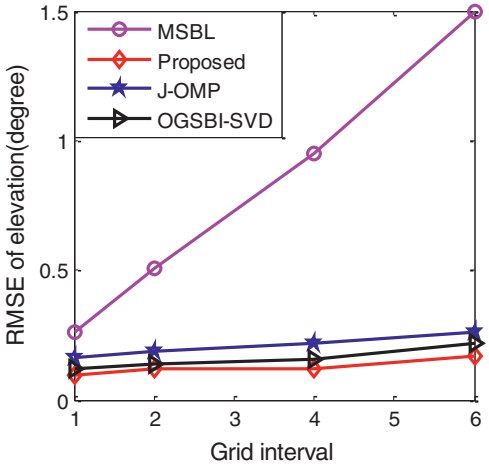

(b) RMSE of elevation versus grid interval

Fig. 4. DOA estimation performance versus grid interval.

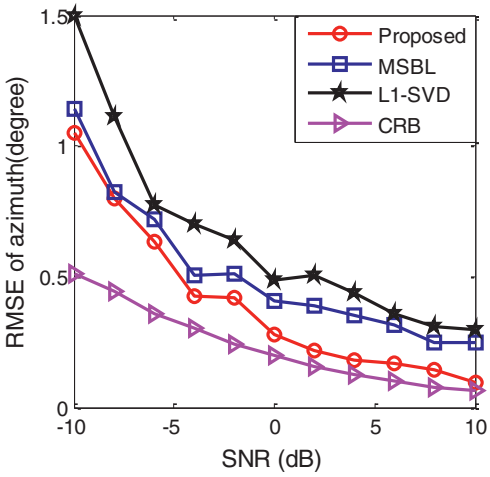

(a) RMSE of azimuth versus SNR

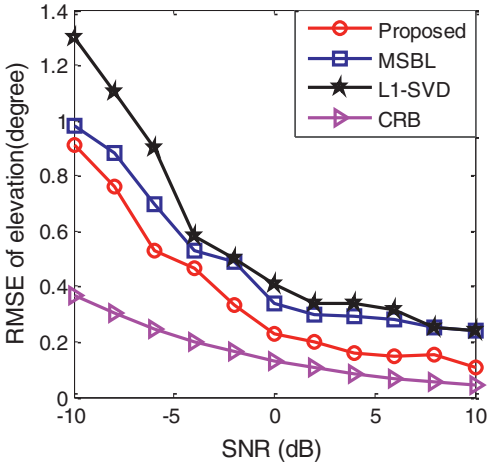

(b) RMSE of elevation versus SNR

Fig. 5. RMSEs of the proposed method and on-grid methods.

4. Simulations

In this section, we present several simulations to show the performance of our proposed method compared with the multiple SBL (MSBL), l_1-SVD algorithm, J-OMP, and OGSBI-SVD. Since the original J-OMP in [22] and OGSBI-SVD in [23] are developed for linear arrays, we make some modifications of these algorithms and extend them to be applicable for spherical arrays. The radius of the spherical array used in the simulations is 0.1 m. There are 32 sensors distributed in a uniform way on the rigid sphere. The maximum order of the spherical harmonics is $N = 4$.

Root mean square error (RMSE) is adopted to evaluate the DOA estimation performance and the RMSEs of all methods are compared to the Cramer-Rao bound (CRB) [37]. In the process of sparse Bayesian learning, we set the maximum number of iterations as 1000 and the tolerance μ as 10^{-3}. We initialize $\langle\gamma\rangle_q = 100T/\sum_{\tau=1}^{2T}\mathrm{var}\{\mathbf{x}_r(\tau)\}$, $\langle\boldsymbol{\alpha}\rangle_q = \sum_{\tau=1}^{2T}|\mathbf{A}_r^{\mathrm{T}}\mathbf{x}_r(\tau)|/2T$, $\boldsymbol{\beta}_1 = \mathbf{0}_H$, $\boldsymbol{\beta}_2 = \mathbf{0}_H$, and $b^{(\alpha)} = c^{(\alpha)} = b^{(\gamma)} = c^{(\gamma)} = 0$.

4.1. Feasibility of the PSBL-LS method

In this part, the snapshot is 200 and the grid interval is set as 2°. First, we compare the estimate accuracy of angular differences $\boldsymbol{\beta}_1$ and $\boldsymbol{\beta}_2$ by LS and EM methods when the posterior distribution of sparse signal $\mathbf{S}_r$ is updated by VSBL method. Two methods achieve similar accuracy seen from Fig. 2. Second, we compare the RMSEs of SBL-LS in Algorithm 1 and PSBL-LS in Algorithm 2. The value of L in Algorithm 2 is set as 2, 4, and 8, respectively. In order to choose the optimal value of L, the RMSEs of azimuth and elevation are shown in Fig. 3. From Fig. 3, we can see the PSBL-LS method in Algorithm 2 with L being 8 can achieve similar performance as that of the real-valued SBL method in Algorithm 1 using all basis functions. Therefore, in the following simulations, we set L as 8 to improve the efficiency of PSBL-LS as well as remain good estimation performance.

4.2. Robustness to the grid intervals

In this part, the influence of different grid intervals is considered. The SNR is set as 5 dB and the snapshot is fixed as 200. The grid interval is set as 1°, 2°, 4°, and 6° respectively. The azimuth angles of two sources are uniformly generated within [60°, 64°] and [110°, 114°] with the interval 0.2° while the elevation angles are uniformly generated within [30°, 34°] and [80°, 84°] with the interval 0.2°. The estimation performance versus grid interval is shown in Fig. 4. From the figures, we can see that the three off-grid methods have better performance than MSBL because these off-grid methods model the angular differences while the on-grid method ignores them. The advantages of the off-grid methods become more obvious in the case of a coarser sampling grid. At the

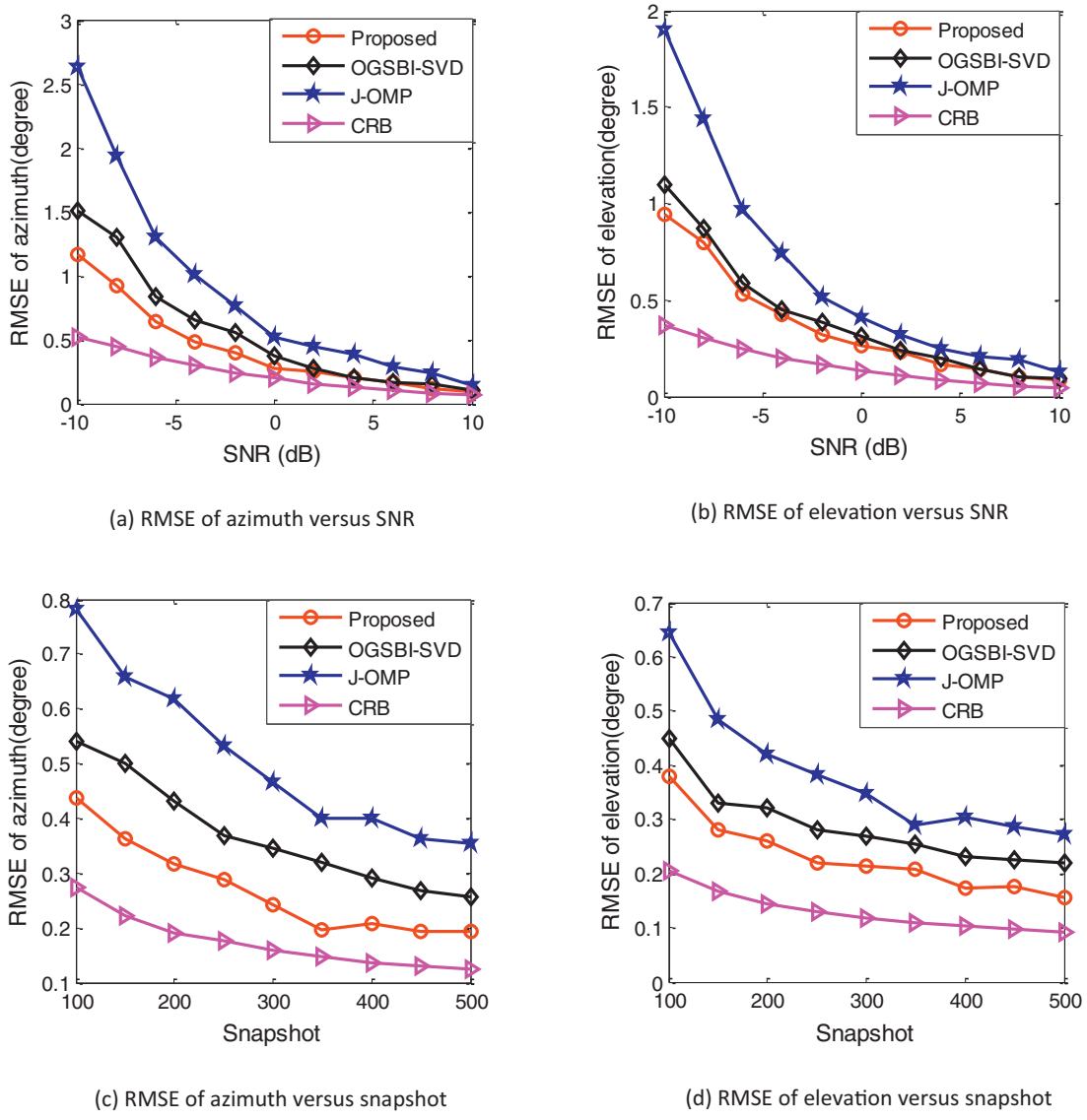

(a) RMSE of azimuth versus SNR

(b) RMSE of elevation versus SNR

(c) RMSE of azimuth versus snapshot

(d) RMSE of elevation versus snapshot

Fig. 6. DOA estimation performance versus SNR and snapshot.

same time, our proposed method achieves more accurate result than J-OMP and OGSBI-SVD methods.

4.3. Compare the proposed method with on-grid methods

In this part, we compare our proposed PSBL-LS method with on-grid MSBL and l_1-SVD algorithms. It aims at illustrating the advantage of our proposed off-grid model that takes the angular differences into consideration. The elevation sampling grid $\theta \in \{0°, r°, 2r°, ..., 180°\}$ and azimuth sampling grid $\phi \in \{0°, r°, 2r°, ..., 360°\}$ are uniform with $r = 1$. The snapshot is 200. Two uncorrelated far-field narrowband signals impinge on the spherical arrays from (50.3°, 60.2°) and (80.7°, 110.8°).

The estimation errors decrease with the increase of SNR seen from Fig. 5. The proposed off-grid model has lower RMSEs than MSBL and l_1-SVD because it considers the differences between the true DOAs and predefined sampling grids. When DOAs do not locate on the predefined sampling grids exactly, MSBL and l_1-SVD only give the nearest grids as the DOA estimations and ignore the differences between the discrete grids and true DOAs.

4.4. Compare the proposed method with different off-grid methods

In this part, we compare our proposed method with two off-grid methods which are J-OMP and OGSBI-SVD. Simulations are performed under different SNRs and snapshots when the interval of grids is set as 4°. The figures (a) and (b) in Fig. 6 are performed with 200 snapshots and the figures (c) and (d) are performed when SNR is 0 dB Through these simulations, it is seen that the performances of all methods get better with the increase of SNRs and the number of snapshots. Our proposed method achieves better accuracy than J-OMP and OGSBI-SVD methods in the same SNR and the snapshot. The reason is that the J-OMP algorithm is based on minimum residual norm, and this method is affected by noises greatly. Different from OGSBI-SVD, we modify the noise variance and signal variance learning rules according to their posterior distributions instead of point estimates, which simplify the problem and improve the accuracy.

4.5. A simplified method

The real spherical harmonics $\bar{g}_n^m$ in (20) have mirror symmetry with respect to azimuth due to the trigonometric function, such

Table 1
Comparison of computational load in one iteration.

Amount \ Main item		RM	RA
CV model	$\mathbf{G}_c^{\mathrm{T}}\mathbf{G}_c$	$4JH^2$	$(4J-2)H^2$
	$\mathbf{G}_c^{\mathrm{T}}\mathbf{X}_c$	$4JHT$	$(4J-2)HT$
	$\mathbf{G}_c\mathbf{S}_c$	$4JHT$	$J(4H-2)T$
RV model	$\mathbf{G}_r^{\mathrm{T}}\mathbf{G}_r$	JH^2	$(J-1)H^2$
	$\mathbf{G}_r^{\mathrm{T}}\mathbf{X}_r$	$2JHT$	$2J(H-1)T$
	$\mathbf{G}_r\mathbf{S}_r$	$2JHT$	$2(J-1)HT$
Simplified RV model	$\mathbf{G}_s^{\mathrm{T}}\mathbf{G}_s$	$0.25JH^2$	$0.25(0.5J-1)H^2$
	$\mathbf{G}_s^{\mathrm{T}}\mathbf{X}_s$	$0.5JHT$	$J(0.5H-1)T$
	$\mathbf{G}_s\mathbf{S}_s$	$0.5JHT$	$(0.5J-1)HT$

that $\bar{g}_n^m(\theta,\phi+\pi)=(-1)^m\bar{g}_n^m(\theta,\phi)$. This property illustrates the real spherical harmonic functions for even values of m are equal to themselves with a phase shift of π along ϕ. Therefore, we can extract even rows of the matching matrix $\mathbf{G}_r$ and the observation matrix $\mathbf{X}_r$ to estimate DOAs. This method can restrict the azimuth $\phi\in\{0°, ..., 180°\}$ instead of $\phi\in\{0°, ..., 360°\}$. And the 180° phase ambiguity can be eliminated by choosing a larger value between ϕ and $\phi+180°$. Fig. 7 shows the accuracy performance of this simplified method when the grid interval is set as 4 and the snapshot is 200. We can see the accuracy of the simplified method is not as good as the proposed method because the extraction has missed some information but the accuracy is still better than J-OMP at the same SNR. Fig. 8 shows the resolution performance of the simplified method. In Fig. 8(a), two uncorrelated far-field narrowband signals impinge on the spherical array from (70.7°, 30.2°) and (70.7°, 40.8°). When $\max_{d=1,2}\{|\hat{\phi}_d-\phi_d|\}$ is less than $|\phi_1-\phi_2|/2$, where $\hat{\phi}_d$ stands for the estimated azimuth for the dth signal, we consider two signals are resolved [25]. In Fig. 8(b), two uncorrelated far-field narrowband signals impinge on the spherical array from (48.7°, 110.2°) and (70.3°, 110.2°). Two signals are resolved if $\max_{d=1,2}\{|\hat{\theta}_d-\theta_d|\}$ is less than $|\theta_1-\theta_2|/2$, where $\hat{\theta}_d$ stands for the estimated elevation for the dth signal. We can see both resolutions of the proposed method and simplified method are better than J-OMP method when the two sources are close to each other.

4.6. Computational cost analysis

First, we discuss the complexity of three models using SBL method to estimate DOAs. They are complex-valued model (CV model), the proposed real-valued model (RV model), and simplified RV model. The main computations of SBL algorithm are decided by matching matrix $\mathbf{G}$ due to its high dimension. The matching matrix $\mathbf{G}$ affects the parameter updates in (35), (36), and (43). Table 1 shows the amount of computations using the three models. In Table 1, $\mathbf{G}_c$, $\mathbf{X}_c$, $\mathbf{S}_c$, $\mathbf{G}_r$, $\mathbf{X}_r$, $\mathbf{S}_r$, and $\mathbf{G}_s$, $\mathbf{X}_s$, $\mathbf{S}_s$ represent matching matrices, received data and sparse signals in CV model, RV model and simplified RV model, respectively.

Real multiplication (RM) and real addition (RA) are used to measure the computational cost of the three models. Our proposed RV model transforms the complex-valued matching matrix into a real-valued one through a unitary transformation without changing the dimension. A unitary transformation $\mathbf{QX}_c$ needs $4J^2T$ RMs and $(4J-2)JT$ RAs and it does not join the iteration of SBL. The computation is very small compared with the reduced computations seen in Table 1, so the computational complexity can be reduced greatly. Furthermore, the simplified RV model uses the mirror symmetry with respect to azimuth of real spherical harmonics and extracts the even rows of matching matrix to estimate DOAs. This method obviously reduces about three quarters computational load compared with using the RV model.

Second, we analyze computational complexity of different DOA estimation methods. In [10], l_1-SVD method is used to estimate DOAs. The computational complexity of l_1-SVD is $\mathcal{O}(D^3H^3)$. J-OMP method is used to solve off-grid targets in ULAs in [22] and computational complexity of J-OMP is $\mathcal{O}(J^2H)$. The computational complexity of OGSBI-SVD method in [23] is $\mathcal{O}(JH^2)$. At the same time, the computational complexity of OGSBI-SVD with basis-pruned approach [30] is $\mathcal{O}(Jp_1^2)$, where $p_1\in[\tilde{L},H]$ is the number of selected basis functions. While the computational complexity of our proposed PSBL-LS method is $\mathcal{O}(Jp_2^2)$, where $p_2\in[L,L+D]$ for different iterations. Because H is much larger than $L+D$ and $\tilde{L}$ is similar to L, therefore our proposed PSBL-LS algorithm is faster than OGSBI-SVD with basis-pruned approach (OGSBI-BP). Table 2 gives the computation time of OGSBI-SVD, OGSBI-BP, and proposed PSBL-LS methods versus the grid interval of azimuth and elevation. The grid in-

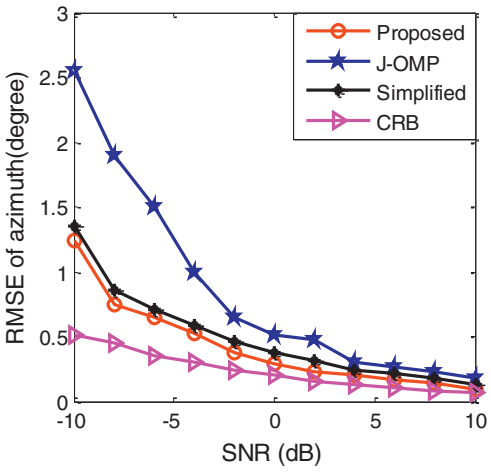

(a) RMSE of azimuth versus SNR

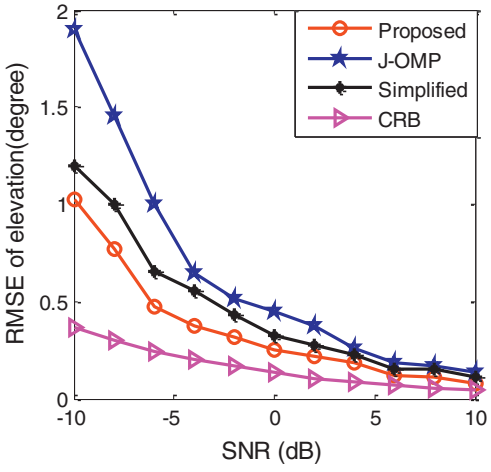

(b) RMSE of elevation versus SNR

Fig. 7. DOA estimation performance of simplified method.

Table 2
Computation time of three off-grid methods.

Grid intervals of azimuth and elevation (°)	Time (sec)		
	PSBL-LS	OGSBI-BP	OGSBI-SVD
(10,5)	0.5	0.8	6.4
(5,2)	1.6	4.5	32.1
(2,1)	6.2	20.4	160.3

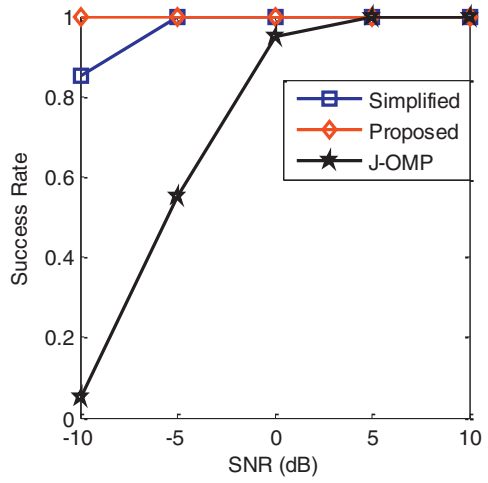

(a) the resolution of azimuth

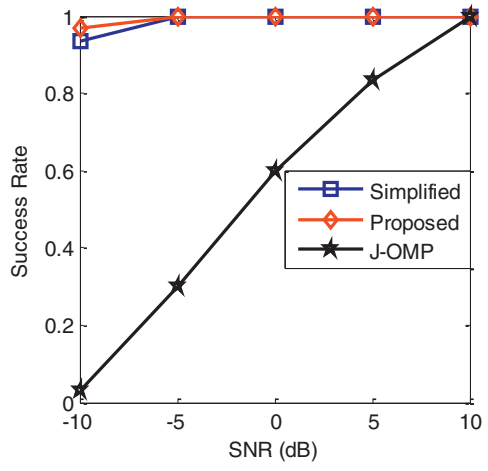

(b) the resolution of elevation

Fig. 8. The resolution of off-grid methods.

tervals of azimuth and elevation are (10°, 5°), (5°, 2°), and (2°, 1°), respectively. The SNR is 10 dB and the snapshot is 200. We can see our proposed PSBL-LS method costs the least time for the same grid interval.

5. Conclusion

In this paper, we construct a 2-D off-grid model in real spherical harmonics domain. The new model keeps joint sparsity between angular differences and sparse signals. Real-valued SBL is used to approximate the posterior density of the sparse signals and the angular differences are estimated by LS method. In order to reduce computations, the PSBL-LS is proposed to estimate 2-D off-grid DOAs. Simulation results show that our proposed method has a better performance than MSBL, l_1-SVD, J-OMP, and OGSBI-SVD methods and is closer to CRB. Moreover, we simplify the real-valued model to further decrease the complexity which can still get better accuracy than J-OMP method. In future work, we are interested to extend the algorithm to wideband signals and consider the mutual coupling between the elements of spherical arrays.

Acknowledgment

The authors would like to thank the editor and anonymous reviewers for their valuable comments. This work was supported by National Natural Science Foundation (61571279), Shanghai Natural Science Foundation (14ZR1415000) of China.

Appendix

Updating angular differences by EM method

We estimate angular differences $\boldsymbol{\beta}_1$ and $\boldsymbol{\beta}_2$ by MAP estimate. An EM algorithm is implemented that treats sparse signal $\mathbf{S}_r$ as a hidden variable and maximizes the cost function $E\{\ln p(\mathbf{X}_r|\mathbf{S}_r, \gamma, \boldsymbol{\beta}_1, \boldsymbol{\beta}_2)p(\boldsymbol{\beta}_1)p(\boldsymbol{\beta}_2)\}$ with respect to $\boldsymbol{\beta}_1$ and $\boldsymbol{\beta}_2$. When the priors of $\boldsymbol{\beta}_1$ and $\boldsymbol{\beta}_2$ are noninformative, maximizing $E\{\ln p(\mathbf{X}_r|\mathbf{S}_r, \gamma, \boldsymbol{\beta}_1, \boldsymbol{\beta}_2)p(\boldsymbol{\beta}_1)p(\boldsymbol{\beta}_2)\}$ is equal to minimize $E\{||\mathbf{X}_r - \mathbf{G}_r\mathbf{S}_r||_{\mathrm{F}}^2\}$.

$$E\left\{||\mathbf{X}_r - \mathbf{G}_r\mathbf{S}_r||_{\mathrm{F}}^2\right\} = \frac{1}{2T}||\mathbf{X}_r - \mathbf{G}_r\mathbf{U}||_F^2 + \mathrm{tr}\left\{\mathbf{G}_r\boldsymbol{\Sigma}\mathbf{G}_r^{\mathrm{T}}\right\} = \boldsymbol{\beta}_1^{\mathrm{T}}\mathbf{P}_1\boldsymbol{\beta}_1 - 2\mathbf{V}_1{}^{\mathrm{T}}\boldsymbol{\beta}_1 + \boldsymbol{\beta}_2^{\mathrm{T}}\mathbf{P}_2\boldsymbol{\beta}_2 - 2\mathbf{V}_2^{\mathrm{T}}\boldsymbol{\beta}_2 + C_3, \tag{50}$$

where C_3 is a constant, $\mathbf{U} = [\mathbf{u}(1), ..., \mathbf{u}(2T)]$, $\mathbf{P}_1$ and $\mathbf{P}_2$ are positive semidefinite matrices

$$\mathbf{P}_1 = (\boldsymbol{\Sigma} + \mathbf{U}\mathbf{U}^{\mathrm{T}}) \odot \mathbf{F}_r^{\mathrm{T}}\mathbf{F}_r, \tag{51}$$

$$\mathbf{P}_2 = (\boldsymbol{\Sigma} + \mathbf{U}\mathbf{U}^{\mathrm{T}}) \odot \mathbf{C}_r^{\mathrm{T}}\mathbf{C}_r, \tag{52}$$

$$\mathbf{V}_1 = \frac{1}{2T}\sum_{\tau=1}^{2T}(diag(\mathbf{u}(\tau))\mathbf{F}_r^{\mathrm{T}}\mathbf{x}_r(\tau) - diag(\mathbf{u}(\tau))\mathbf{F}_r^{\mathrm{T}}\mathbf{A}_r\mathbf{u}(\tau)) - diag(\mathbf{F}_r^{\mathrm{T}}\mathbf{A}_r\boldsymbol{\Sigma}) - \frac{1}{2}\left\{\frac{1}{2T}\sum_{\tau=1}^{2T}diag(\mathbf{u}(\tau))\mathbf{F}_r^{\mathrm{T}}\mathbf{C}_r diag(\mathbf{u}(\tau)) - (\boldsymbol{\Sigma} \odot \mathbf{F}_r^{\mathrm{T}}\mathbf{C}_r)^{\mathrm{T}}\right\}\boldsymbol{\beta}_2 \quad , \tag{53}$$

$$\mathbf{V}_2 = \frac{1}{2T}\sum_{\tau=1}^{2T}(\mathrm{diag}(\mathbf{u}(\tau))\mathbf{C}_r^{\mathrm{T}}\mathbf{x}_r(\tau) - \mathrm{diag}(\mathbf{u}(\tau))\mathbf{C}_r^{\mathrm{T}}\mathbf{A}_r\mathbf{u}(\tau)) - \mathrm{diag}(\mathbf{C}_r^{\mathrm{T}}\mathbf{A}_r\boldsymbol{\Sigma}) - \frac{1}{2}\left\{\frac{1}{2T}\sum_{\tau=1}^{2T}\mathrm{diag}(\mathbf{u}(\tau))\mathbf{C}_r^{\mathrm{T}}\mathbf{F}_r\mathrm{diag}(\mathbf{u}(\tau)) - (\boldsymbol{\Sigma} \odot \mathbf{C}_r^{\mathrm{T}}\mathbf{F}_r)^{\mathrm{T}}\right\}\boldsymbol{\beta}_1. \tag{54}$$

In order to minimize (50), we compute its partial derivatives with respect to $\boldsymbol{\beta}_1$ and $\boldsymbol{\beta}_2$. By letting partial derivatives equal to zeroes, the results of $\boldsymbol{\beta}_1$ and $\boldsymbol{\beta}_2$ can be achieved as

$$\boldsymbol{\beta}_1 = \frac{\mathbf{V}_1}{\mathbf{P}_1}, \quad \boldsymbol{\beta}_2 = \frac{\mathbf{V}_2}{\mathbf{P}_2}. \tag{55}$$

References

[1] H. Krim, M. Viberg, Two decades of array signal processing research: the parametric approach, IEEE Signal Process. Mag. 13 (4) (1996) 67–94.
[2] A. Boukerche, H. Oliveira, E. Nakamura, A. Loureiro, Localization systems for wireless sensor networks, IEEE Trans. Wirel. Commun. 14 (6) (2007) 6–12.
[3] R. Schmidt, Multiple emitter location and signal parameter estimation, IEEE Trans. Antennas Propag. 34 (3) (1986) 276–280.
[4] R. Roy, T. Kailath, ESPRIT-estimation of signal parameters via rotational invariance techniques, IEEE Trans. Acoust., Speech Signal Process 37 (7) (1989) 984–995.
[5] J. Tropp, A. Gilbert, Signal recovery from partial information via orthogonal matching pursuit, IEEE Trans. Info. Theor. 53 (12) (2007) 4655–4666.
[6] R. Tibshirani, Regression shrinkage and selection via the Lasso, J. Royal Statist. Soc. 58 (1) (1996) 267–288.
[7] J. Chen, X. Huo, Theoretical results on sparse representations of multiple-measurement vectors, IEEE Trans. Signal Process 54 (12) (2006) 4634–4643.

[8] B. Wang, J. Liu, X. Sun, Mixed sources localization based on sparse signal reconstruction, IEEE Signal Process. Lett. 19 (8) (2012) 487–490.
[9] B. Jeffs, Sparse inverse solution methods for signal and image processing applications, in: Proceedings of IEEE International Conference on Acoustics, Speech and Signal Processing, 3, 1998, pp. 1885–1888.
[10] D. Malioutov, M. Cetin, A. Willsky, A sparse signal reconstruction perspective for source localization with sensor arrays, IEEE Trans. Signal Process. 53 (8) (2005) 3010–3022.
[11] D. Wipf, B. Rao, An empirical Bayesian strategy for solving the simultaneous sparse approximation problem, IEEE Trans. Signal Process. 55 (7) (2007) 3704–3716.
[12] S. Ji, Y. Xue, L. Carin, Bayesian compressive sensing, IEEE Trans. Image Process 56 (6) (2008) 2346–2356.
[13] S. Babacan, R. Molina, A. Katsaggelos, Bayesian compressive sensing using Laplace priors, IEEE Trans. Image Process. 19 (1) (2010) 53–63.
[14] Z. Zhang, B. Rao, Sparse signal recovery with temporally correlated source vectors using sparse Bayesian learning, Sel. Top. Signal Process. 5 (5) (2011) 912–926.
[15] T. Bendory, S. Dekel, A. Feuer, Super-resolution on the sphere using convex optimization, IEEE Trans. Signal Process. 63 (9) (2015) 2253–2262.
[16] Y. Chi, Y. Chen, Compressive two-dimensional harmonic retrieval via atomic norm minimization, IEEE Trans. Signal Process. 63 (4) (2015) 1030–1042.
[17] Z. Yang, L. Xie, P. Stoica, Vandermonde decomposition of multilevel Toeplitz matrices with application to multidimensional super-resolution, IEEE Trans. Info. Theor. 62 (6) (2016) 3685–3701.
[18] Z. Yang, L. Xie, C. Zhang, A discretization-free sparse and parametric approach for linear array signal processing, IEEE Trans. Signal Process. 62 (19) (2014) 4959–4973.
[19] Z. Tan, Y. Eldar, A. Nehorai, Direction of arrival estimation using co-prime arrays: a super resolution viewpoint, IEEE Trans. Signal Process. 62 (21) (2014) 5565–5576.
[20] Z. Yang, L. Xie, On gridless sparse methods for multi-snapshot DOA estimation, in: Proceedings of the 41st IEEE International Conference on Acoustics, Speech and Signal Processing (ICASSP 2016), shanghai, China, 2016 March 20-25.
[21] H. Zhu, G. Leus, G. Giannakis, Sparsity-cognizant total least-squares for perturbed compressive sampling, IEEE Trans. Signal Process 59 (5) (2011) 2002–2016.
[22] Z. Tan, A. Nehorai, Sparse direction of arrival estimation using co-prime arrays with off-grid targets, IEEE Signal Process. Lett. 21 (1) (2014) 26–29.
[23] Z. Yang, L. Xie, C. Zhang, Off-grid direction of arrival estimation using sparse Bayesian inference, IEEE Trans. Signal Process 61 (1) (2013) 38–43.
[24] Y. Zhang, Z. Ye, X. Xu, N. Hu, Off-grid DOA estimation using array covariance matrix and block-sparse Bayesian learning, Signal Process 98 (2014) 197–201.
[25] J. Dai, X. Xu, D. Zhao, Direction-of-arrival estimation via real-valued sparse representation, IEEE Antennas Wirel. Propag. Lett. 12 (2013) 376–379.
[26] J. Dai, W. Xu, D. Zhao, Real-valued DOA estimation for uniform linear array with unknown mutual coupling, Signal Process. 92 (2012) 2056–2065.
[27] W. Si, X. Qu, Z. Qu, et al, Off-grid DOA estimation via real-valued sparse bayesian method in compressed sensing, Circuits Syst. Signal Process. (2016) 1–17
[28] Q. Huang, G. Zhang, Y. Fang, Real-valued DOA estimation for spherical arrays using sparse Bayesian learning, Signal Process 125 (2016) 79–86.
[29] M. Carlin, P. Rocca, G. Oliveri, Directions-of-arrival estimation through Bayesian compressive sensing strategies, IEEE Trans. Antennas Propag. 61 (7) (2013) 3828–3838.
[30] D. Shutin, T. Buchgraber, S. Kulkarni, et al., Fast variational sparse Bayesian learning with automatic relevance determination for superimposed signals, IEEE Trans. Signal Process. 59 (12) (2011) 6257–6261.
[31] S. Lei, W. Huali, Direction-of-arrival estimation based on modified Bayesian compressive sensing method, in: Proceedings of the IEEE International Conference on Wireless Communications and Signal Processing (WCSP), 2011.
[32] D. Khaykin, B. Rafaely, Coherent signals direction-of-arrival estimation using a spherical microphone array: frequency smoothing approach, IEEE Workshop Appl. Signal Process. Audio Acoust. WASPAA'09 (2009) 221–224.
[33] B. Rafaely, Analysis and design of spherical microphone arrays, IEEE Trans. Speech Audio Process 13 (1) (2005) 135–143.
[34] Q. Huang, T. Wang, Acoustic source localization in mixed field using spherical microphone arrays, EURASIP J. Adv. Signal Process. 1 (2014) 1–16 (2014).
[35] R. Goossens, H. Rogier, 2-D angle estimation with spherical arrays for scalar fields, Signal Process. IET 3 (3) (2009) 221–231.
[36] H. Sun, S. Yan, U. Svensson, Robust spherical microphone array beamforming with multi-beam-multi-null steering, and sidelobe control, IEEE Workshop Appl. Signal Process. Audio Acoust. WASPAA'09 (2009) 113–116.
[37] L. Kumar, R. Hegde, Stochastic Cramér-Rao bound analysis for DOA estimation in spherical harmonics domain, IEEE Signal Process. Lett. 22 (8) (2015) 1030–1034.
[38] B. Rafaely, in: Fundamentals of Spherical Array Processing, Springer, 2015, p. 10.
[39] D. Shutin, T. Buchgraber, S. Kulkarni, H. Poor, Fast variational sparse Bayesian learning with automatic relevance determination for superimposed signals, IEEE Trans. Signal Process 59 (12) (2011) 6257–6261.
[40] C. Fox, S. Roberts, A tutorial on variational Bayesian inference, Artif. Intell. Rev. 38 (2) (2012) 85–95.
[41] S. Chatterjee, K. Hari, P. Händel, et al., Projection-based atom selection in orthogonal matching pursuit for compressive sensing, in: Proceedings of the IEEE National Conference on Communications (NCC), 2012.